Microstructural characteristics and thermophysical properties of spark plasma sintered Inconel 738LC

O. F. Ogunbiyi, T. Jamiru, E. R. Sadiku, L. W. Beneke, O. T. Adesina & T. A. Adegbola

The International Journal of Advanced Manufacturing Technology

ISSN 0268-3768

Int J Adv Manuf Technol
DOI 10.1007/s00170-019-03983-w

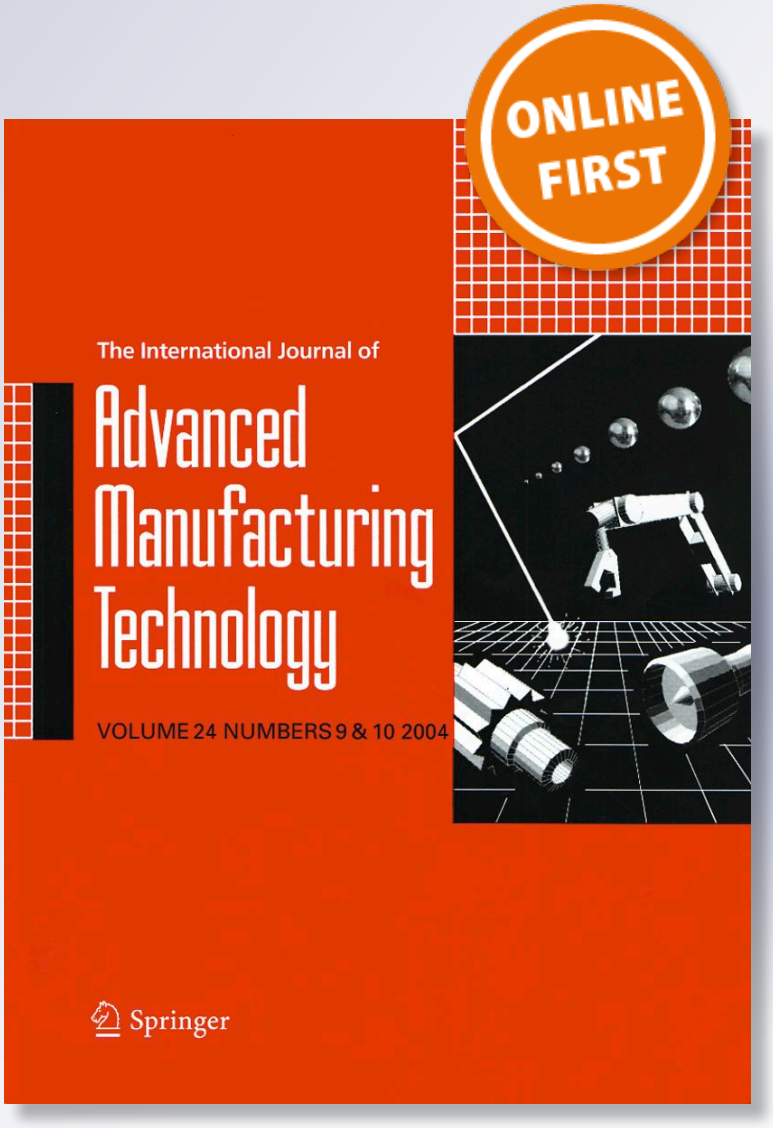

Springer

The International Journal of Advanced Manufacturing Technology
https://doi.org/10.1007/s00170-019-03983-w

ORIGINAL ARTICLE

Microstructural characteristics and thermophysical properties of spark plasma sintered Inconel 738LC

O. F. Ogunbiyi[1] · T. Jamiru[1] · E. R. Sadiku[2] · L. W. Beneke[1] · O. T. Adesina[1] · T. A. Adegbola[1]

Received: 3 April 2019 / Accepted: 3 June 2019

Abstract
Nickel-based superalloys are used for turbine component parts in the power industry, aircraft engines, and in the marine sector. One such alloy that is available for these purposes is Inconel 738LC (IN738LC) nickel-based superalloy. Therefore, it is pertinent to have good structural and thermal stabilities for high-temperature applications, since these characteristics are important for its performance. In this study, spark plasma sintering technology was used to fabricate IN738LC nickel-based superalloy by using sintering temperature in the range of between 900 and 1200 °C. The fabricated products were characterized by using the scanning electron microscope and X-ray diffraction. There was the formation of the $\gamma'(Ni_3(Ti, A\ell))$ intermetallic phase in the microstructure, which contributed to the material (Inconel 738LC) property. The solid solution elements present are chromium, cobalt, tungsten, and tantalum; these equally contribute to the structural stability of IN738LC. The density, hardness, and the predicted yield strength increased with increasing sintering temperature, while the porosity decreased with increasing sintering temperature. The thermal conductivity, which is an important thermophysical property of IN738LC, enables the evaluation of the usefulness and service life of IN738LC superalloy at high-temperature applications, was also examined. The thermal conductivity was measured by using a laser flash method in the temperature range of 100–600 °C. For the sintered alloy, the thermal conductivity was determined as a function of the thermal diffusivity, specific heat capacity, and density. Analysis showed inflection pattern with increase in temperature on the sample fabricated at 900, 1000, and 1100 °C, ; a monotonic increase with increase in temperature was observed on the sample fabricated at 1200°C, ; the inflections are associated with the γ' precipitates dissolution and redistribution.

Keywords IN738LC · Spark plasma sintering · Microstructure · Laser flash · Thermal diffusivity · Thermal conductivity

✉ O. F. Ogunbiyi
olugbengaogunbiyi@gmail.com

T. Jamiru
jamiruT@tut.ac.za

E. R. Sadiku
sadikur@tut.ac.za

L. W. Beneke
BenekeLW@tut.ac.za

O. T. Adesina
oluwagbengaadesina@yahoo.com

T. A. Adegbola
adesolaAT@tut.ac.za

[1] Department of Mechanical Engineering, Mechatronics and Industrial Design, Tshwane University of Technology, Pretoria, South Africa

[2] Institute for NanoEngineering Research (INER) and Department of Chemical, Metallurgical and Materials Engineering, Tshwane University of Technology, Pretoria, South Africa

1 Introduction

The process of power generation is a complex one due to the high temperature steam/gas that is commonly used to power the turbines. This has necessitated the use of high strength structural materials that can withstand the harsh environment created, in order to enable the turbines to perform efficiently and optimally. A typical gas/steam turbine requires temperature of over 500 ° C for its operation [1], and this creates an aggressive environment for the component parts of the turbines. Therefore, nickel-based superalloys are materials that have found applications in this environment. This is due to their ability to acclimatize to stringent operating conditions. They are suitable for both high temperature or cryogenic environments and they possess good material and mechanical properties, such as good oxidation resistance, high thermal stability at elevated temperatures, excellent hot corrosion resistance in an aggressive environment of sulfur, carbon, and

Published online: 04 July 2019

nitrogen [2, 3], resistance to fatigue and good creep-rupture property [4, 5]. One of the promising superalloy candidates is the Inconel 738LC (IN738LC) nickel-based superalloy, IN738LC, which has large number of elements within its makeup and it is predominantly a solid solution-strengthened material that has enormous potentials to function at elevated temperature working environments. The constituent elements that form the alloy can be divided into three groups, viz: the first groups are those elements that are similar in characteristics with the matrix nickel element; these are Cr and Co. The second group is the 'heavy metals' group, such as Ta and W. They are high-temperature solid solution-strengthened elements, which usually impact hardness strength on the alloy. The third group contains Ti and Aℓ, which form the intermetallic precipitate γ' phase (Ni_3 (Ti, Aℓ)); it has L1 structure and often similar to the fcc γ matrix phase; nevertheless, the intermetallic phase (γ') can improve the material properties by precipitating within the microstructure in order to impede dislocation movement [6].

Fabricating a nickel-based superalloy can be a daunting task, because of the high qualities that are demanded of the alloy, both in mechanical and physical properties. Therefore, it is imperative for metallurgists and material scientists to find alternative means to the conventional processing techniques to produce superalloys [7, 8]. It is in these lights that powder metallurgy production route is embraced as alternative. It is a material production technology that has several advantages over the conventional processes, e.g., vacuum arc melting (VAR) friction stir method and vacuum induction melting (VIM) [9–14]. These include the production of materials with good dimensional stability, fast production processes, clean energy with minimal human contact, ease of reproducibility, material with better mechanical properties and minimal inherent defects. The technology ensures the development of solid materials that combine good physical and mechanical properties in a one-step of production, such as the reduction of micro-segregation, pinholes, pores, excessive grain growth, impurities and inclusions, and the reduction of these draw backs promote microstructure homogeneity. Therefore, spark plasma sintering is one of the most recent technologies in powder metallurgy that come with several advantages, such as grain refinement, homogenous elemental distribution, near-uniform heat distribution during sintering, formation, and distribution of secondary phase precipitates (for alloys that are prone to precipitate formation or intermetallic phase formation) [15]. In addition, are micro-segregation elimination, porosity reduction, and good surface-finished properties [16]. It is a method that employs the use of direct electrical current of low voltage and uniaxial force (under low atmospheric pressure), to advance powder consolidation and also makes possible, fast sintering of elemental powders. SPS combines powder consolidation and densification in one-step during operation and the diffusion mechanism is characterized by the use of intense heating and rapid cooling sequentially, a process that accelerates densification and reduction of grain growth. Although SPS technology has been used by different researchers to manipulate microstructure characteristics of a nickel-based superalloy [17] for some specific application, on that account, the stability of thermo-mechanical properties, such as thermal conductivity, diffusivity, and the specific heat capacity of IN738LC alloy at high temperature, is tied to the intermetallic precipitate and the solid solution strengthening element formed. These properties remain a disadvantage, because they cause internal stress to the nickel-based superalloy [18].

Furthermore, thermal conductivity is an important physical property that helps to evaluate and predict the useful life of nickel-based superalloy. Therefore, by developing a material that has high ability for rapid heat transfer when exposed to a high thermal radiating environment is an obvious necessity. This mechanism will enable the fast cooling, which will ultimately prolong the lifespan of a material and also regulate the occurrence of life-limiting heat attack spot. In addition, a material with high thermal conducting property will improve uniform temperature distribution and, by extension, reduce thermally induced stresses and temperature gradient; hence, this will appreciably improve the creep-rupture and fatigue strength properties [3, 19]. Laser flash is a machine used for measuring thermal properties of solids, liquids, and powder materials. The technique involves the heating of the front side of a square dimension graphite-coated specimen, by a short energy laser pulse; the temperature penetrates the specimen and thermal conductivity is measured on the rear surface as a function of time by using an infrared detector. The specimen is placed in the tube furnace, while the analysis is underway.

Few studies are available on the use of laser flash analysis in order to determine the thermal conductivity of nickel-based superalloy. Among the report available is an investigation of the thermal properties of cast nickel-based superalloys [18] and the thermal analysis of coated nickel-based superalloy with ceramic by using the thermal spraying technique [20, 21]. In this study, thermo-physical properties and microstructure of SPS IN738LC nickel-based superalloy sintered at 900, 1000, 1100, and 1200 ° C are analyzed, using SEM, XRD, and laser flash analysis. The thermophysical data obtained in the present study have been analyzed in the light of very scarce available literature information.

2 Experimental procedure

2.1 Materials

Seven different metallic powders were used in this study in order to produce the IN738LC nickel-based superalloy; nickel powder (particle size range from 45 to 90 μm, 99.5% purity) was supplied by TLS-TechnikGmbh, Germany. This served as

the matrix element, while other metallic powders serve as the constituent elements in different proportions. This is shown in Table 1. These powders are chromium and cobalt (particle size range from 3 to 44 μm, 99.9% purity) supplied by Alfa Aesar, tungsten, titanium, and tantalum (particle size range from 3 to 44 μm, 99% purity) supplied by Sigma-Aldrich, South Africa. The aluminum used (particle size of 25 μm, 99.8% purity) was supplied by TLS-TechnikGmbh, Germany. All the powder particles were spherical in shape and had a near zero contamination when they were delivered. Weighing scale was used to measure the quantity required of each powder into a bottle, in preparation for mixing. This was done according to the stoichiometric composition of IN738LC nickel-based superalloy [22]. A turbula mixer was used to mix the powders together for a period of 12 h at a speed of 49 rpm in a dry environment. This is to ensure a homogenous distribution of individual elemental powder in the matrix Ni powder. At the completion of mixing, it was poured into a graphite die, ready for sintering.

2.2 Sintering

The Spark plasma sintering (SPS) machine (HHPD 25 manufactured by FCT Germany) was used for this experiment. A 59.5 g of admixed powder was poured into the graphite die of 40 mm diameter and the sample specification is a 6 mm thickness by Ø 40 mm. Graphite foil (0.3 mm thickness) was placed between the die inner surface and the sample in order to prevent the specimen from having direct contact with the die and the punches (insulation). This is necessary in order to ensure clean sintering process. Prior to the starting of the sintering process, degassing was done in order to create a vacuum environment in the heating chamber (oxygen-free atmosphere). A control thermocouple was fixed at the lower punch, 2 mm below the sample chamber. The schematic setup of spark plasma sintering system is shown in Fig. 1. The sintering parameters were set at 50 MPa pressure, 100 k/min heating rates, and 5 min holding time, while the sintering temperature was varied over four different set values (900, 1000, 1100, and 1200 °C). These are represented by using symbols **a, b, c**, and **d**, and subsequently in this report, **a, b, c**, and **d** will be used to represent the sample products. The sintering activities were recorded by the pyrometer and at the completion, while cooling was activated and the samples were removed. Sandblasting was done in order to remove the deposited carbon on the surface of the samples.

Table 1 Percentage constituent of IN738LC

Material	Ni	Cr	Co	Ti	Aℓ	W	Ta
Percentage (%)	64.58	16	8.3	3.4	3.4	2.6	1.72

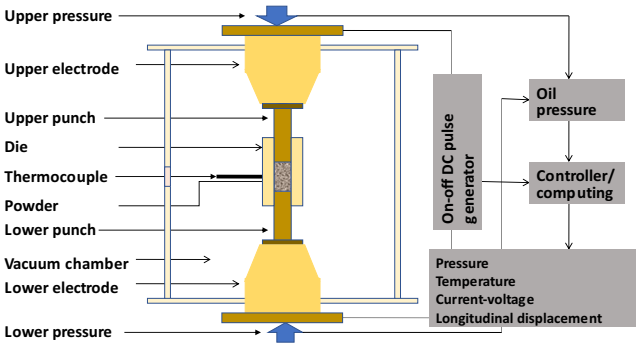

Fig. 1 Schematic setup of spark plasma sintering system

2.3 Characterization and mechanical properties spark plasma sintering IN738LC alloys

The sintered IN738LC samples were characterized by using a Falcon 500 series polarizing optical microscope (POM), field emission scanning electron microscope (SEM) (JEOL JSM-7600F SEM), which was incorporated with an EDS detector with a INCA X-Stream2 pulse analyzer software. An X-ray diffraction (XRD) machine, a model from PANalytical Empyrean with CuKα radiation, characterized the phases present in the samples. The XRD result was further simplified by using a Highscore plus software to analyze the data. Prior to scanning on the electron microscope (SEM), the materials were sectioned for metallographic examinations. Each sample was metallographically prepared [23]; grinding and polishing were done (in the order of 600, 800, 1200 grit size silicon carbide papers, while 0.004 mm colloidal silica was used for polishing) in order to obtain a mirror surface. Carpenter reagent was used as etchant to enable clear view of the microstructure (etchant composition; 2 g of $CuCl_2$, 50 ml of HCl, 25 ml of HNO_3, and 200 ml of H_2O). The theoretical density and the relative densities of the sintered samples were evaluated, and the micro-hardness values were determined by using a Vickers hardness testing machine, at an applied load of 500 g force for a period of 10 s each. It was repeated 10 times for accuracy purpose, while the average mean value was taken to be the actual hardness value. A relationship between the ultimate tensile strength and yield strength with respect to the Vickers hardness strength was reported by Osada et al. [24]. The Vickers hardness (Hv) values were used in the eq. 1 in order to obtain the predicted yield strength (YS) of the sintered samples in MPa. Osada et.al [25] validated this equation and stated that the equation is valid for nickel-based superalloy with Vickers hardness value approximately in the range of $100 \leq Hv \leq 400$. Therefore, eq. 1 was adopted [24] to compute the YS of the sintered IN738LC (least value of Hv in this

study is 144 and the highest is 362).

$$YS = 2.46\ Hv \quad (1)$$

2.4 Thermal analysis

The thermal properties of the IN738LC nickel-based superalloy were investigated and are shown in Table 2. The measurements were taken at room temperature for both density and thermal diffusivity, while the specific heat capacity used is the value reported by Nipera Technology data [26, 27] for IN738LC nickel-based superalloy. Equation (2) shows the relationship between the thermal conductivity, thermal diffusivity, density, and specific heat capacity for solid material, and this is used to compute thermal conductivity values for the sintered samples. The four samples were analyzed, while the diffusivity test was conducted by using the NETZSCH model 427 laser flash diffusivity apparatus. Figure 2 shows the schematic diagram of the measuring part of a NETZSCH Laser Flash 457 equipment. The specification of the sample's dimensions used for the thermal analysis test is 10 mm × 10 mm × 4 mm.

$$\lambda = \rho.\mathbb{C}_p.a \quad (2)$$

Where

λ thermal conductivity
ρ Bulk density
$\mathbb{C}_p$ Specific heat capacity
a Thermal diffusivity

The setup comprises of a high temperature water-cooled furnace that has the capacity to analyze a material up to 2000 °C. The samples were examined in the furnace chamber of the machine, while nitrogen which is an inert gas was used to create a non-reactive atmosphere; the sample chamber (furnace) is separated from the graphite element by a protective tube. Pulsed energy from the laser is exacted on the sample front surface, the laser voltage used is 450 V, and the laser pulse with is 0.8 ms. The alloy (IN738LC) was able to absorb the heat due to the good thermal conductivity it possesses. The heat diffuses through the sample thickness and results to the increase in the temperature of the sample back surface; this is measured by an IN-Sb detector with respect to time. Data recording and evaluation were done by a PC software package that is attached to the equipment. The LFA 427 operating process followed in this experiment was in accordance with ASTM E-1461 standard. The thermal diffusivity measurement was conducted under argon and nitrogen condition from room temperature to 600 °C. The samples were of equal dimensions and they were coated with graphite on both surfaces (front and back) in order to facilitate the absorption of flashlight on the front's surface; this also increases the emissivity on the sample's backside.

3 Results and discussion

3.1 Microstructural analysis

Figure 3 shows the optical micrographs for the four sintered alloys; the micrographs exemplify the information on the surface morphology of the etched samples, including the pores present. Figure 3a–d represents the samples sintered at 900, 1000, 1100, and 1200 °C. Colored annotation is used for a clear understanding of the sample's topography; hence, the grains and the grain boundaries can be seen, and this is obvious in the sample sintered at 900 °C. The images show an admixture of white patches and gray/dark patches; they were later confirmed by the SEM micrograph (Fig. 4), to be rich chromium area and other solid solution strengthening elements, such as tantalum and tungsten. The grain structure that was observed from sample A is spheroidal and of big size; this later changed in the other samples as the sintering temperature increases. This signifies the fact that a 900°C sintering temperature is not sufficient for an effective particle deformation, because the smaller the grain size the better the material is and by extension, the mechanical properties developed in the material [29].

Furthermore, the occurrence in sample A (sintered at 900 °C) means that the powder particle only displayed a slight plasticity, i.e., the energy supplied at 900 °C is not sufficient to plastically deformed the powder particle and to cause grain refinement. As the sintering temperature increases, few dark

Table 2 Summary of samples properties

Samples	SPS (°C)	TD (g/cm^2)	ED (g/cm^2)	RD (%)	P (%)	MH (Hv)	PYS (MPa)
IN738LC (A)	900	7.894	7.396	93.69	6.31	144.5	355.5
IN738LC (B)	1000	7.894	7.574	95.95	4.05	186.47	458.7
IN738LC (C)	1100	7.894	7.609	96.39	3.61	255.46	628.4
IN738LC (D)	1200	7.894	7.801	98.82	1.18	362.25	891.1

SPS spark plasma sintering temperature, *TD* theoretical density, *ED* experimental density, *RD* relative density, *P* porosity, *MH* microhardness, *PYS* predicted yield strength

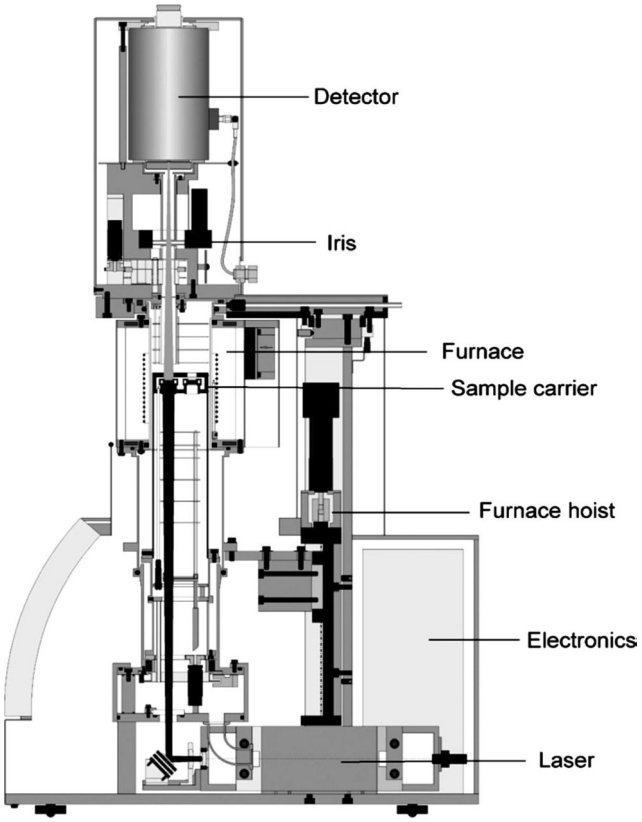

Fig. 2 Measurement part of the NETZSCH LFA 457 MicroFlash [28]

spots were observed, which is suspected to be pores and the percentage porosity, with respect to the density of the sintered alloys, will be further discussed in the later part of this report.

The pores were seen to be separated from each other, which is beneficial to the alloy [30]. The grains show a non-spheroidal structure on the alloy sintered above 900 °C, which signifies the fact that the powder particles have been plastically deformed as it undergoes transition. This is the reason why the highest density was obtained with sample D (98.82%), while the sample sintered at 900°C, recorded the least density (93.69%). Finer grains with very few dark spots were observed on the sample D (sintered at 1200°C).

Figure 4 shows the SEM micrographs of the surface topographies for the etched samples, sintered at 900°*C* (a), 1000 °C (b), 1100 ° C (c), and 1200°C (d). On the micrographs, scanty pores were observed, while the precipitation of solid solution strengthening element occurred and this was confirmed by XRD analysis, as shown in the Fig. 4a. There were clear distinctions between grains and grain boundaries. Grain was observed to be the areas that were dominated by the occurrence of precipitated intermetallic phases, as shown in Fig. 4b. Three clear distinct features were seen, viz: the first is the scanty pores within the microstructure, the second is the formation of γ'-precipitated intermetallic phase, which is randomly dispersed within the matrix. It was observed that the intermetallic phase overlapped on the γ matrix phase and this is not surprising because it agrees with the XRD analysis. The third feature is the precipitated solid solution strengthening element, which is observed to be a tantalum and tungsten. They appear in the form of light gray patches on the micrograph; these light gray patches, when analyzed, showed that they were the precipitated solid solution strengthening element, which are tungsten and tantalum and they appear to be present in large percentages, according to the EDX analysis. The

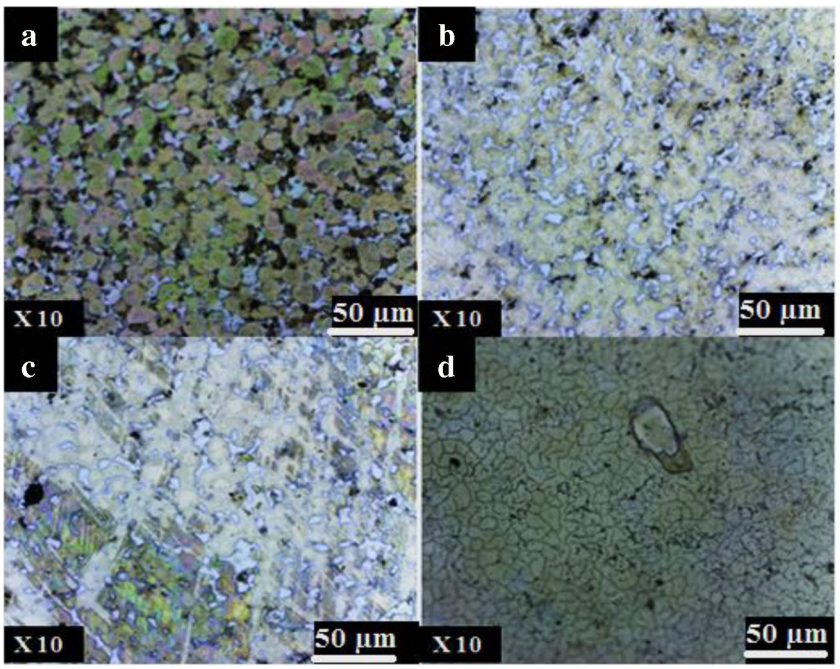

Fig. 3 OPM microstructure of IN738LC: **a** 900 ° C, **b** 1000 ° C, **c** 1100 ° C, and **d** 1200 ° C

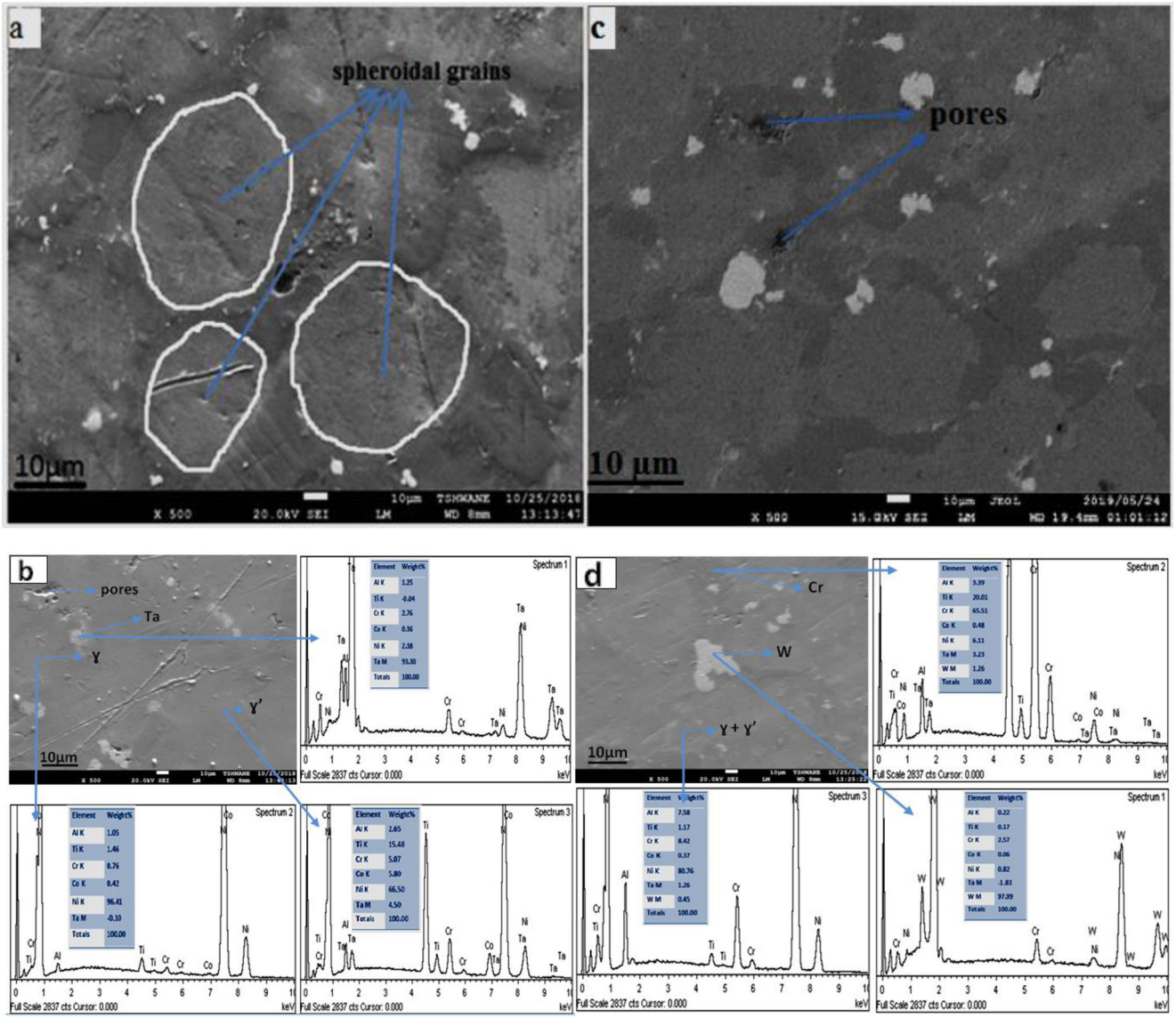

Fig. 4 SEM microstructure and EDX analysis of IN738LC sintered at **a** 900 ° C, **b** 1000 ° C, **c** 1100 ° C, and **d** 1200 ° C

chromium, which is an element that is known to impact corrosion and oxidation resistance properties, could be seen along the grain boundary of the $\gamma + \gamma'$ precipitate; an indication that the material produced will have good oxidation and corrosion resistance properties [31]. Tungsten and tantalum are hard heavy metals, which are beneficial to this type of alloy (IN738LC). Their presence imparts hardness characteristic on the super alloy and impede movement of dislocation lines. The grains and the precipitated solid solution strengthening elements were not observed to be of equal size and orientation; this is an advantage to the sintered alloy, because it will contribute to the appreciable densification enjoyed by the sintered alloys. The γ' intermetallic phase that is present is in agreement with previous studies [31, 32].

3.2 XRD analysis

The phase constituents for the sintered IN738LC superalloy were identified by XRD analysis and are illustrated in Fig. 5. The samples were sintered at 900°C, 1000°C, 1100°C, and 1200°C. The phases formed and the crystallographic plane were observed and reported, accordingly. The peaks of the

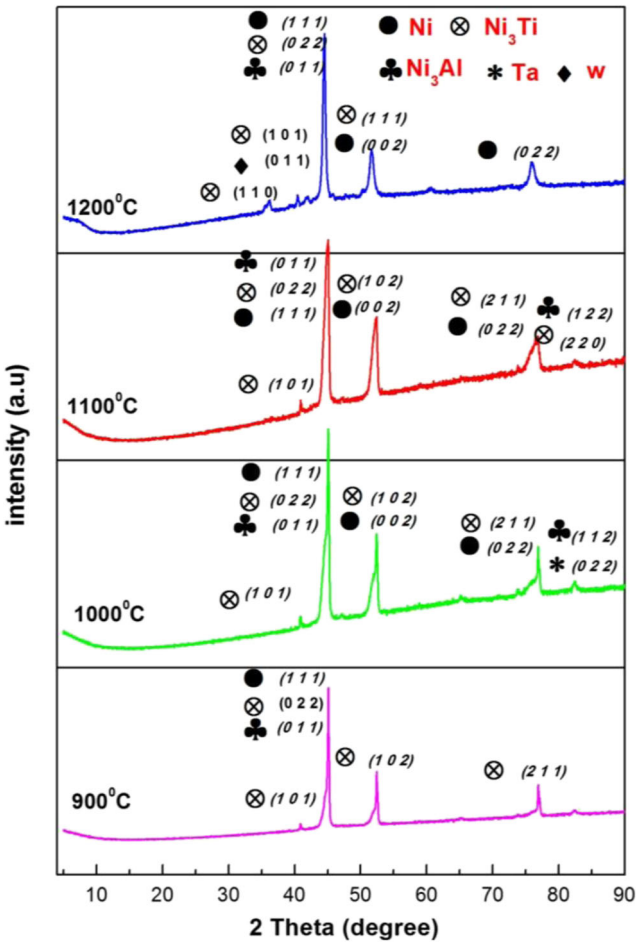

Fig. 5 XRD patterns of the sintered IN738LC at 900, 1000, 1100, and 1200 °C

phases and the solid solution elements present were observed, and the dominant phases present in all the samples after the γ matrix phase are the coherent precipitated γ′ (Ni_3(Ti, Aℓ)) intermetallic phase and the precipitation of Ta and W solid solution strengthening element. These phases were revealed from the sample sintered at 1000°C and 1200°C. They are hard heavy metals that contribute to the material properties. The γ′ (Ni_3(Ti, Aℓ)) intermetallic phase occurred at four different Bragg's angles (2θ), in the samples sintered at 900 and 1200°C. This is different for the other two sintering temperatures, where the phase appeared at five different Bragg's angle (2θ) for the samples sintered at 1000 and 1100°C. It was difficult to separate the peaks where γ and γ′ occurred due to the overlap of the peaks and this is not a coincidence, since this phenomenon had been reported in the past [33, 34].

In a study conducted by Sarkar et al., a similar case was observed; the peaks obtained for the matrix phase and intermetallic secondary phase from XRD analysis, were observed to overlap [35]. Furthermore, it was also observed that there is an increase in the intensity, as the sintering temperature increases, particularly at 2θ = 44°Bragg's angle, a situation that is attributed to an increase in the formation and precipitation of the intermetallic phase within the matrix. The peaks were identified at diffraction angles of 2θ = 36°, 42°, 44°, 52°, 76°, and 82°, while the major peaks were at angle 2θ = 44° and 52°. The peaks at 2θ = 36°, 42°, and 82° appeared to be minor peaks, while at 2θ = 44°, 52° appeared to be major peaks. Peak at 2θ = 76° is relatively obvious, but not as potent as those at 2θ = 44° and 52°. A γ-phase was observed in all the samples at angle 2θ = 44° (1 1 1), 52° (0 0 2), 76° (0 0 2), for the samples sintered at 1000, 1100, and 1200°C. Tungsten (W) was observed at 2θ = 42° (0 1 1) in the sample sintered at 1200°C, Tantalum (Ta) was observed at 2θ = 82° (0 2 2) in the sample sintered at 1000°C. The γ′ (Ni_3Aℓ) phase peak was at 2θ = 44° (0 1 1) in all the samples and at 2θ = 82° (1 1 2) for samples sintered at 1000 and 1100°C. γ′ (Ni_3Ti) was dominant in the intermetallic phase that overlapped with both γ matrix and γ′. In the Ni_3Aℓ intermetallic phase, this was observed at 2θ = 36°(1 1 0) for the sample sintered at 1200°C and at 2θ = 42°, 44° (1 0 1), (0 0 2) for all the samples. This occurred at angle 2θ = 52° (1 0 2) for the samples sintered at 900, 1000, and 1100°C and at 2θ = 76° (2 1 1) for samples sintered at 900, 1000, and 1100°*C*, while 2θ = 82° (2 2 0) for sample sintered at 1100°C. Slight peak broadening was observed, especially at angle 2θ = 52° and 76°. This signifies the elemental decomposition and grain size reduction and is expected to favor densification and should also improve material properties.

3.3 Relative density, porosity, micro-hardness, and yield strength of the sintered IN738LC alloy

The results for the theoretical density, relative density, percentage porosity, micro-hardness, and calculated yield strength of sintered IN738LC alloys are summarized in Table 2. Equation 3 was used to obtain the theoretical density in this experiment and the relative density (density after sintering) was obtained by using Archimedes' method. The porosity of the sintered IN738LC alloys was determined [36] by using eq. 4.

$$TD = 1 \div \left(\frac{weight\%ofelementA}{densityofsampleA} + \frac{weight\%ofelementB}{densityofsampleB} + \text{——} + \frac{weight\%ofelementn!}{densityofsamplen!}\right) \quad (3)$$

$$P = 100 - \left(\frac{ED}{TD} \times 100\right) \quad (4)$$

where P = porosity, ED = experimental density, and TD = theoretical density.

The sintering temperature used was varied over four values, i.e., from 900 to 1200 °C. It was observed that the alloy behaved differently; therefore, this shows the importance of sintering temperature as one of the SPS parameters that influence the properties of a material. The alloy density increased as the sintering temperature increased, and a maximum density was obtained for the alloy sintered at 1200 °C.

There is a relationship between material densification property and the level of the inherent porosity during fabrication. This study shows that an increase in density leads to a decrease in the percentage of the pores formed within the alloy. The least percentage pore was found in the alloy sintered at 1200 °C, which was 1.18% at a density of 98.82%. The percentage porosity was in the order of 6.32, 4.05, 3.61, and 1.18% for the alloys sintered in the order of 900, 1000, 1100, and 1200 °C. The density was in the order of 93.69, 95.95, 96.39, and 98.83 g/cm^3, with increasing sintering temperature. The results obtained are presented in Table 3**.** In addition, Fig. 6 shows the comparison between density and porosity, with respect to sintering temperature. The increase in density and decrease in porosity influence the hardness property of the sintered alloy. There was an increase in the hardness values as the sintering temperature increased and this is summarized in Table 3. However, the higher relative density observed in the alloy sintered at 1200 °C, is attributed to the good densification of the alloy; this is close to the theoretical density of 7.894 g/cm^3.

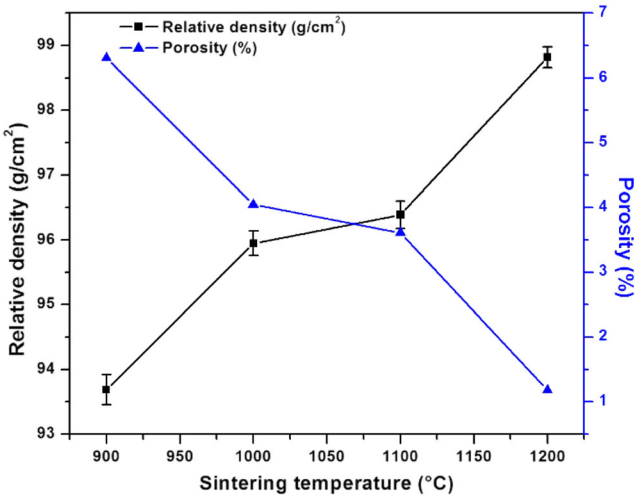

Fig. 6 The relative density and porosity of the sintered IN738LC alloys

Table 3 Thermal diffusivity, thermal conductivity, and specific heat of superalloy In738LC as a function of temperature

Temperature, °C	Thermal diffusivity, mm^2/s	Specific heat, J/(g·K) [26, 27]	Thermal conductivity, W/(m·K)
Superalloy: In738LC-density: 7.396 g/cm^3 A			
100	8.88	0.460548	30.247
200	8.27	0.502416	30.730
300	7.76	0.52335	30.037
400	8.18	0.544284	32.929
500	8.31	0.565218	34.739
600	8.55	0.586152	37.066
Superalloy: In738LC-density: 7.574 g/cm^3 B			
100	4.70	0.460548	16.394
200	4.85	0.502416	18.456
300	4.77	0.52335	18.908
400	5.21	0.544284	21.478
500	5.43	0.565218	23.246
600	5.83	0.586152	25.882
Superalloy: In738LC-density: 7.609 g/cm^3 C			
100	3.67	0.460548	12.861
200	3.83	0.502416	14.641
300	4.09	0.52335	16.287
400	4.42	0.544284	18.305
500	4.47	0.565218	19.224
600	5.27	0.586152	23.504
Superalloy: In738LC-density: 7.801 g/cm^3 D			
100	4.48	0.460548	16.095
200	4.98	0.502416	19.518
300	5.54	0.52335	22.618
400	6.06	0.544284	25.731
500	6.47	0.565218	28.528
600	7.31	0.586152	33.426

The yield strength (YS) for the alloys was predicted from the hardness values recorded, by using eq. 1. It was observed that the predicted YS increased with increase in the sintering temperature and this is presented in Table 3. The increase is attributed to the good densification during alloy fabrication and the precipitation of solid solution strengthening elements: Ta, Cr, and W within the microstructure. Ta and W were observed to have precipitated within the matrix as gray patches on the microstructure, while Cr was observed to have formed along the grain boundaries, as shown in Fig. 4, while the intermetallic γ' ($Ni_3(A\ell, Ti)$ phase that was observed overlapped on the γ (Ni) matrix (Fig. 5), was homogenously distributed. Since aluminum and titanium are known to have lower densities when compared to other constituent elements present, they promoted precipitation of the intermetallic compound, which impacted strength on the sintered alloy. They occupied the vacancies and the interstices within the microstructure and hence, they minimized voids formation. The high value of the predicted YS observed can also be ascribed to the precipitation of the intermetallic and solid solution strengthening phases. In Fig. 6, the linear progression of the increase in the relative density and the decrease in percentage porosity was shown. It should be noted that the increase in density, micro-hardness and decrease in porosity observed in this study were similar to that obtained by Khouzani et al. [37]. In their study, sintering temperatures of 950, 1000, 1050, 1075, and 1100 °C were used for the experiment. The porosity observed indicated that the alloy sintered at 950 °C had 22.5% porosity, followed by 16% for alloy sintered at 1000 °C and 3% for that sintered at 1050 °C, while the other two sintering temperatures experienced a "met-out". The marginal difference in their work and this study can be explained; thus, they employed cobalt superalloy, while this work was on nickel superalloy; also, some sintering parameters, e.g., pressure and holding time, can contribute to the marginal differences. Similar trend was observed for micro-hardness values, i.e., an increase in the sintering temperatures led to increases in the micro-hardness values. Jose et al. [38] in their study on SPS of nickel superalloy, using sintering temperatures of 900, 950, 1000, and 1050 °C reported also that increase in sintering temperature improved the hardness property, improved material consolidation, and reduced the percentage porosity. This is quite similar to the result obtained in this study.

3.4 Thermal diffusivity and thermal conductivity measurement

The thermal behavior, with respect to change in the thermal diffusivity, thermal conductivity, and specific heat capacity of IN738LC superalloy, as a function of temperature was measured by using laser flash method (Fig. 7). Table 3 represents the thermophysical properties (thermal diffusivity, thermal conductivity, and specific heat capacity) data emanating from the analysis. This was conducted at a temperature range of between 100 and 600°C, while the thermal diffusivity was measured at discrete isothermal temperatures, at an interval of 100°C. It was obvious from Fig. 7 that the thermal diffusivity, thermal conductivity, and specific heat increased with increasing temperature for all the samples, except the sample sintered at 900°*C*. For this alloy sample, the thermophysical value initially decreased from 100- to 300°C, and later, it started to increase. A major observation on the linear progression graph, for the thermophysical properties as a function of temperature, was the point of inflections at some specific temperatures. This was observed in all the samples, except the sample sintered at 1200°C. For instance, in the sample sintered at 1000 and 1100°C, the distinct inflection points were observed at 300°C and 500°C, while the sample sintered at 1200°C exhibited a monotonous pattern (linear progression) for the thermophysical properties as the temperature increased. The sample sintered at 900°C clearly showed an abnormal pattern, even though an inflection point was observed at 300°C. There can be a whole lot of reasons that are responsible for this behavior. A major factor is believed to be associated with some phase transformation occurrences and structural adjustment (disordering in the matrix phase and atomic redistribution). This can lead to the unexpected decrease in the diffusivity and conductivity properties, with increase in temperature, in the sintered IN738LC alloy. The dissolution of precipitated γ' intermetallic and γ matrix phases might be the phenomenon that occurred at the points of inflection. In addition, element such as Cr will precipitate [1] at temperatures of between 477 and 667°C and Cr precipitation along grain boundaries was observed from the microstructure (Fig. 4).

Furthermore, a couple of defects and internal stress may be part of what causes the behavior observed. For a clear understanding, Arun et al. [1] stated, in a similar study, that the thermal diffusivity test, by using laser flash, may not be enough to state the phenomenon that transpired at the point of inflections. Therefore, a further characterization, by using differential scanning calorimetry (DSC), was carried out. They observed that five transformation peaks occurred, and they employed the Thermo-Cal software with TCNi7 database to study the reaction/phase transformation that occurred, including the starting point to the finishing point. Another reported [39, 40] cause of inflections is the dissolution of the γ' precipitated phase at a certain temperature. This phenomenon occurs as a function of some elemental constituents (Ti, Aℓ, Cr). In this study, it was observed, from the microstructure studies, i.e., EDX and XRD that the phases formed were the precipitation of $\gamma + \gamma'$ phase and some precipitation of the solid solution strengthening elements. Therefore, the inflection points observed as the thermophysical properties increased with increase in temperature can be correlated to the dissolution of γ and γ' phases, dissolution of Cr, and some other elements (Ti, Aℓ).

The mechanisms that lead to the increase in the thermophysical properties with increase in temperature can

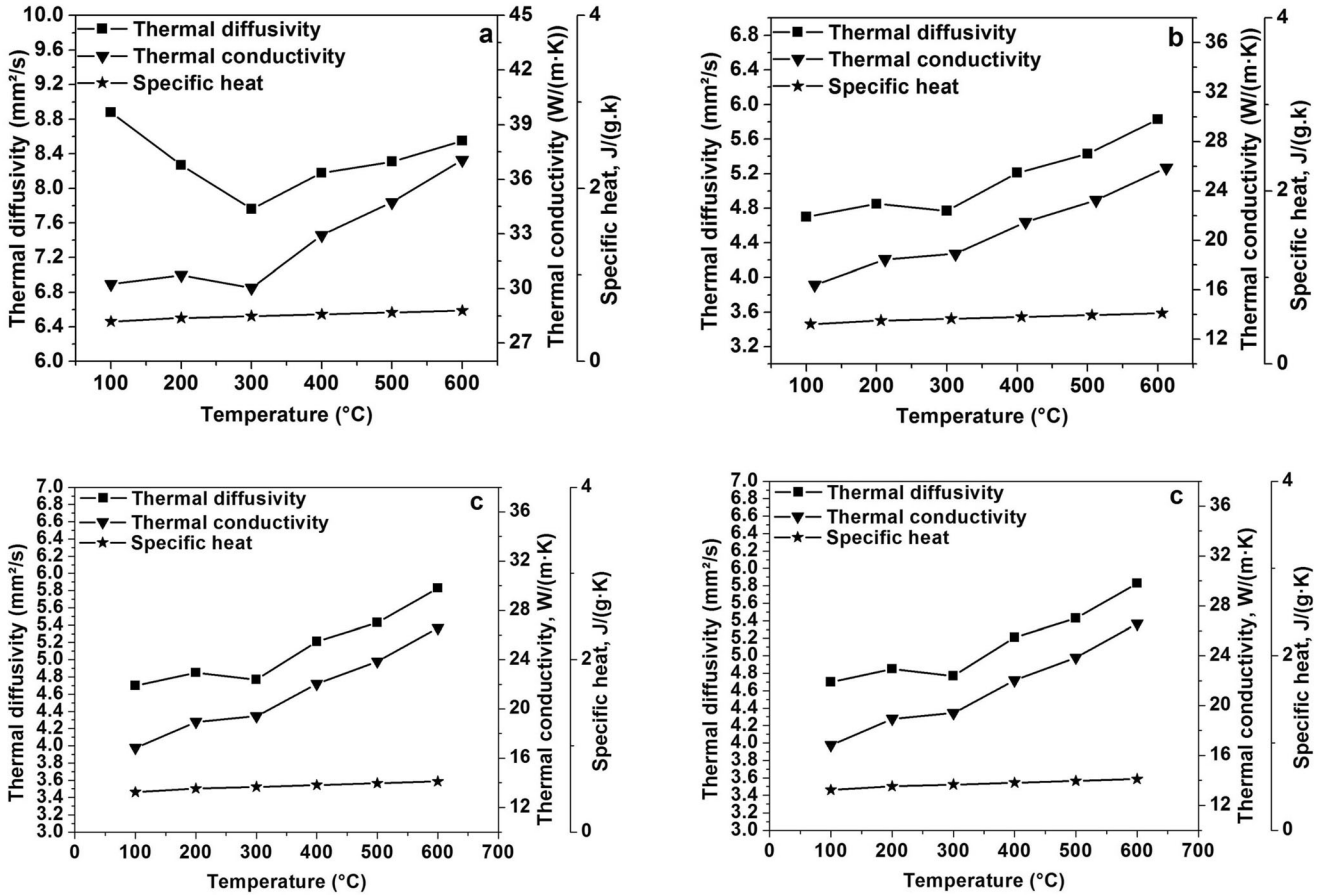

Fig. 7 Thermal diffusivity, thermal conductivity, and specific heat of superalloy IN738LC as a function of temperature, sintered at **a** 900°C, **b** 1000°C, **c** 1100°C, **d** 1200°C

be explained in detail; thus, the fundamental conservation of thermal energy in metallic alloy is via the electrons and phonons or phonon waves. Due to these two parameters, the total thermal conductivity of a metallic material has two components, which are expressed [41] as follows:

$$K_t = K_l + K_e \tag{5}$$

where K_l is the lattice contribution occurrence due to the heat transport of phonon or phonon waves and K_e is the electronic contribution. However, it has been reported that the major contributor to the total thermal conductivity behavior of a metallic material is the electronic component, while the lattice effect is deemed minor [41]. Due to the important role played by the electronic component, it can be further expressed as follows.

$$K_e = \frac{LT}{\rho_e} \tag{6}$$

Where L is the Lorenz constant and ρ_e is the electronic resistivity. From eq. 6, it was apparent that there is a linear relationship between electronic thermal conductivity and temperature. However, the experimental study does not, in totality, follow this equation. This always shows a deviation of the electronic thermal conductivity due to changes in either the electronic resistivity or from the Lorentz number. This is because of the different scattering processes [1], since the Lorentz number can either decrease or increase with temperature because of the surface smearing that emerges. This is attributed to the electro-electron scattering and the decrease in the Lorentz number, which is attributed to the electro-phonon scattering. It should be noted that impurity addition and magnetic ordering may contribute to the increase in the electronic resistivity [42, 43]. Consequently, the thermal conductivity of a metallic material is largely dependent on the factors mentioned. Therefore, careful consideration of these factors plays a role in establishing the contribution of the electronic factor [44]. In addition, the representation of the lattice thermal conductivity of most material, above ambient temperature, is given as the following expression:

$$K_t = \frac{1}{\left(A + B^* T^n\right)} \; with \; 0.5 < n < 1 \tag{7}$$

In the eq. (7), the coefficients A and B are constant, and they account for the defect and phonon-phonon scattering. The defect

and photon-photon scattering are accounted for by the constants A and B, as shown in eq. (7). With the decrease in temperature, it becomes obvious that the thermal conductivity decreases due to lattice vibration. This decrease is attributed to the photon-photon increase and also to the photon-defect scattering due to temperature, which in turn, results in the decrease in the heat transfer from one end of the material to the other, under a temperature gradient. Hence, the total thermal conductivity can be written as follows (eq. 8), by combining eqs. 6 and 7.

$$K_t = \left(\frac{LT}{\rho_e}\right) + \left\{\frac{1}{\left(A + B^* T^n\right.}\right\} \tag{8}$$

From eq. 8, the decrease or increase of the total thermal conductivity with temperature depends on the dominance of either the electronic or lattice contribution. From the eq. (9), the temperature dependence of IN738LC can be summarized; thus, it was observed that the sample sintered at 900°C, had its thermal diffusivity decreased at first with increase in temperature, which later picked up at 300 °C. This is attributed to the effect of defect, however small it may be, which increases the electronic resistivity and in turn, resulted to the total thermal conductivity that has been governed by the electronic component alone when compared to the lattice contribution at high temperature. Equation (8) clearly shows that the thermal conductivity will increase with increase in temperature; also Lorentz number should increase with increase in temperature due to Fermi surface smearing [41].

4 Conclusion

In this work, the microstructure of spark plasma sintered Inconel738LC (Ø 40 mm) of a nickel-based superalloy, sintered at temperatures 900, 1000, 1100, and 1200 °C, was investigated and characterized by using SEM and XRD. The thermophysical properties, vis-à-vis, thermal conductivity, thermal diffusivity, and specific heat capacity, were measured as a function of temperature by using the laser flash method. Therefore, the following conclusions were drawn:

(1) The microstructure of the sintered samples, on the account of SEM and XRD analyses, revealed the formation of γ matrix phase, γ' precipitate, and precipitation solid solution strengthening elements, i.e., W, Cr, and Ta. The coherent γ' precipitate represents the secondary intermetallic phase that impacts strength to the sintered IN738LC. These precipitates were found dispersed within the γ matrix and the XRD diffractogram shows an overlapping of the two phases at the same Bragg's angle (2θ) of diffraction. Pores and micro-voids were observed within the morphology. These were found to have light effects on the thermophysical properties.

(2) The thermal diffusivity and thermal conductivity were measured by using the information of alloy 738LC density and specific heat, at the temperature range of 100–600°C; the results were computed. The thermal conductivity increased from 30 $Wm^{-1}k^{-1}$to 37 $Wm^{-1}k^{-1}$ (sintered at 900°C), 16 $Wm^{-1}k^{-1}$ to 25 $Wm^{-1}k^{-1}$(sintered at 1000 °C), 12 $Wm^{-1}k^{-1}$ to 23 $Wm^{-1}k^{-1}$ (sintered at 1100°C), and from 16 $Wm^{-1}k^{-1}$ to 33 $Wm^{-1}k^{-1}$ (sintered at 1200°C).

(3) The relative density, porosity, hardness, and the predicted yield strength were analyzed, and it was discovered that an increase in the sintering temperature improved the material densification and in turn, there were increases in density, hardness and predicted yield strength. Alloy sintered at 1200 °C poses the best mechanical and physical properties.

(4) The thermal conductivity of IN738LC, sintered at four different temperatures (900, 1000, 1100, and 1200°C) by using the spark plasma sintering technology, has been evaluated from the knowledge of thermal diffusivity, heat capacity, and density. The role of alloying element, intermetallic phases, and the defect on the thermal conductivity of IN738 at different temperature domains has been established, based on the available thermal conductivity theories for metal alloys.

(5) The present thermophysical property database generated for IN738LC in the temperature range of between 100 and 600 °C, is expected to provide new inputs to simulate solidification and to guide in the process of selecting appropriate heat treatment parameters. This will enable a succinct evaluation of microstructural stability for long-term material performance, especially in the area of power generation that operates within this temperature range.

Funding information This work is funded by the Research and Innovation Directorate of Tshwane University of Technology and supported, in part, by the Department of Mechanical Engineering, Mechatronics and Industrial Design, Institute for NanoEngineering Research (INER), Department of Chemical, Metallurgical and Materials Engineering and the Faculty of Engineering and Built Environment of the Tshwane University of Technology, Pretoria, South Africa.

References

1. Rai AK, Trpathy H, Hajra R, Raju S, Saroja S (2017) Thermophysical properties of Ni based super alloy 617. J Alloys Compd 698:442–450
2. Balikci E, Raman A (2000) Characteristics of the γ' precipitates at high temperatures in Ni-base polycrystalline superalloy IN738LC. J Mater Sci 35:3593–3597
3. Suwardie JH, Artiaga R, Mier JL (2002) Thermal characterization of a Ni-based superalloy. Thermochim Acta 392:295–298
4. Bugge J, Kjaer S, Blum R (2006) High-efficiency coal-fired power plants development and perspectives. Energy 31:1437–1445

5. Bogner S, Ivanova E, Müller M, Wang F, Ma D, Bührig-Polaczek A (2015) Investigation of the Undercoolability of Ni-based alloys using high temperature thermal analysis. Metals 5:1971–1983
6. Mills KC, Youssef YM, Li Z, Su Y (2006) Calculation of thermophysical properties of Ni-based superalloys. ISIJ Int 46:623–632
7. Mirjavadi SS, Alipour M, Hamouda A, Givi MB, Emamy M (2014) Investigation of the effect of Al-8B master alloy and strain-induced melt activation process on dry sliding wear behavior of an Al–Zn–mg–cu alloy. Mater Des 53:308–316
8. Afshari BM, Mirjavadi SS, Dolatabad YA, Aghajani M, Givi MKB, Alipour M et al (2016) Effects of pre-deformation on microstructure and tensile properties of Al—Zn—mg—cu alloy produced by modified strain induced melt activation. Trans Nonferrous Metals Soc China 26:2283–2295
9. Matysiak H, Zagorska M, Andersson J, Balkowiec A, Cygan R, Rasinski M, Pisarek M, Andrzejczuk M, Kubiak K, Kurzydlowski K (2013) Microstructure of Haynes® 282® superalloy after vacuum induction melting and investment casting of thin-walled components. Materials 6:5016–5037
10. Zupanič F, Bončina T, Križman A, Tichelaar F (2001) Structure of continuously cast Ni-based superalloy Inconel 713C. J Alloys Compd 329:290–297
11. Xu X, Ward R, Jacobs M, Lee P, McLean M (2002) Tree-ring formation during vacuum arc remelting of INCONEL 718: part I. experimental investigation. Metall Mater Trans A 33:1795–1804
12. Mirjavadi SS, Alipour M, Hamouda A, Matin A, Kord S, Afshari BM et al (2017) Effect of multi-pass friction stir processing on the microstructure, mechanical and wear properties of AA5083/ZrO2 nanocomposites. J Alloys Compd 726:1262–1273
13. Hoseinlaghab S, Mirjavadi SS, Sadeghian N, Jalili I, Azarbarmas M, Givi MKB (2015) Influences of welding parameters on the quality and creep properties of friction stir welded polyethylene plates. Mater Des 67:369–378
14. Mirjavadi SS, Alipour M, Emamian S, Kord S, Hamouda A, Koppad PG et al (2017) Influence of TiO2 nanoparticles incorporation to friction stir welded 5083 aluminum alloy on the microstructure, mechanical properties and wear resistance. J Alloys Compd 712:795–803
15. Ghosh N, Harimkar S (2012) Consolidation and synthesis of MAX phases by spark plasma sintering (SPS): a review. In: Advances in science and Technology of Mn+ 1axn phases. Elsevier, pp 47–80
16. Diouf S, Molinari A (2012) Densification mechanisms in spark plasma sintering: effect of particle size and pressure. Powder Technol 221:220–227
17. Ma S, Yang Y, Li A, Zhou S, Shi L, Wang S, Liu M (2018) Effects of temperature on microstructure and mechanical properties of IN718 reinforced by reduced graphene oxide through spark plasma sintering. J Alloys Compd 767:675–681
18. Zieliñska M, Yavorska M, Porêba M, Sieniawski J (2010) Thermal properties of cast nickel based superalloys. Arch Mater Sci Eng 44: 35–38
19. Terada Y, Ohkubo K, Miura S, Sanchez JM, Mohri T (2003) Thermal conductivity and thermal expansion of Ir3X (X= Ti, Zr, Hf, V, Nb, ta) compounds for high-temperature applications. Mater Chem Phys 80:385–390
20. Akoshima M, Tanaka T, Endo S, Baba T, Harada Y, Kojima Y, Kawasaki A, Ono F (2011) Thermal diffusivity measurement for thermal spray coating attached to substrate using laser flash method. Jpn J Appl Phys 50:11RE01
21. Loshchinin YV, Folomeikin YI, Pakhomkin S (2016) A study of the heat capacity of coated metal materials by the laser flash method. Inorg Mater 52:1478–1482
22. Rani S, Agrawal AK, Rastogi V (2017) Failure analysis of a first stage IN738 gas turbine blade tip cracking IN a thermal power plant. Case Stud Eng Fail Anal 8:1–10
23. Pérez-González F, Garza-Montes-de Oca N, Colás R (2014) High temperature oxidation of the Haynes 282© nickel-based superalloy. Oxid Met 82:145–161
24. Osada T, Gu Y, Nagashima N, Yuan Y, Yokokawa T, Harada H (2013) Optimum microstructure combination for maximizing tensile strength in a polycrystalline superalloy with a two-phase structure. Acta Mater 61:1820–1829
25. Osada T, Gu YF, Nagashima N, Yuan Y, Yokokawa T, Harada H (2012) New quantitative analysis of contributing factors to strength of disk SUPERALLOYS. John Wiley & Sons, Chichester
26. Technical Data – NiPERA. One New York plaza, New York, NY, 10004
27. IN-738 Alloy - Preliminary Data (497) - Nickel Institute. One new york plaza, New York, NY, 10004
28. Min S, Blumm J, Lindemann A (2007) A new laser flash system for measurement of the thermophysical properties. Thermochim Acta 455:46–49
29. Furrer D, Fecht H (1999) Ni-based superalloys for turbine discs. Jom 51:14–17
30. Vervoort P, Vetter R, Duszczyk J (1996) Overview of powder injection molding. Adv Perform Mater 3:121–151
31. Wikstrom N, Ojo O, Chaturvedi M (2006) Influence of process parameters on microstructure of transient liquid phase bonded Inconel 738LC superalloy with Amdry DF-3 interlayer. Mater Sci Eng A 417:299–306
32. Jalilvand V, Omidvar H, Shakeri H, Rahimipour M (2013) Microstructural evolution during transient liquid phase bonding of Inconel 738LC using AMS 4777 filler alloy. Mater Charact 75:20–28
33. Zhen J, Li F, Zhu S, Ma J, Qiao Z, Liu W, Yang J (2014) Friction and wear behavior of nickel-alloy-based high temperature self-lubricating composites against Si3N4 and Inconel 718. Tribol Int 75:1–9
34. Özgün Ö, Gülsoy HÖ, Yılmaz R, Fındık F (2013) Microstructural and mechanical characterization of injection molded 718 superalloy powders. J Alloys Compd 576:140–153
35. Sarkar A, Mukherjee P, Barat P, Jayakumar T, Mahadevan S, Rai SK (2008) Lattice misfit measurement in Inconel 625 by X-ray diffraction technique. Int J Modern Phys B 22:3977–3985
36. Eze AA, Jamiru T, Sadiku ER, Durowoju MO, Kupolati WK, Ibrahim ID, Obadele BA, Olubambi PA, Diouf S (2018) Effect of titanium addition on the microstructure, electrical conductivity and mechanical properties of copper by using SPS for the preparation of cu-Ti alloys. J Alloys Compd 736:163–171
37. Khouzani MK, Bahrami A, Mehr MY (2019) Spark plasma sintering of Stellite®-6 superalloy. J Alloys Compd 782:461–468
38. García JMJ, Li Z, Vahlas C, de La Torre SD, López FJ (2010) Spark plasma sintering and characterization of NiCoCrAlY-Ta superalloy powder. J Mater Sci Eng 4:57–63
39. Yang L, Chang K-M, Mannan S, deBarbadillo J (1997) A new DTA approach for verifying precipitate solvus in Inconel alloy 718. Superalloys 718, 625, 706and various derivatives:353–365
40. Yang L, Chang K-M, Mannan S, deBarbadillo J (1997) A new DTA approach for verifying precipitate solvus in Inconel alloy 718(differential thermal analysis). Superalloys 718, 625, 706 and various derivatives:353–365
41. Klemens P, Williams R (1986) Thermal conductivity of metals and alloys. Int Metals Rev 31:197–215
42. Rao K, Åström H, Johannesson C (1972) Magnetic contribution to thermal conductivity of neodymium. Phys Lett A 42:53–55
43. Korenblit IY, Lazarenko YP (1971) Thermal emf and thermal resistance of ferromagnetic metals with impurities. Sov Phys Jetp 33:837–842
44. Murashov V, White M, Tritt T (2004) Thermal conductivity: theory, properties, and applications. Kluwer Academic/Plenum Publishers, New York